J. Fluid Mech. (2000), *vol.* 418, *pp.* 265–295. Printed in the United Kingdom

© 2000 Cambridge University Press

Three-dimensional MHD flows in rectangular ducts with internal obstacles

By B. MÜCK[1], C. GÜNTHER[1], U. MÜLLER[1] AND L. BÜHLER[1]

[1]Forschungszentrum Karlsruhe, Institut für Kern- und Energietechnik, Postfach 3640, D-76021 Germany

(Received 14 October 1999 and in revised form 24 January 2000)

This paper presents a numerical simulation of the magnetohydrodynamic (MHD) liquid metal flow around a square cylinder placed in a rectangular duct. In the hydrodynamic case, for a certain parameter range the well-known Kármán vortex street with three-dimensional flow patterns is observed, similar to the flow around a circular cylinder. In this study a uniform magnetic field aligned with the cylinder is applied and its influence on the formation and downstream transport of vortices is investigated. The relevant key parameters for the MHD flow are the Hartmann number M, the interaction parameter N and the hydrodynamic Reynolds number, all based on the side length of the cylinder. The Hartmann number M was varied in the range $0 \leqslant M \leqslant 85$ and the interaction parameter N in the range $0 \leqslant N \leqslant 36$. Results are presented for two fixed Reynolds numbers $Re = 200$ and $Re = 250$. The magnetic Reynolds number is assumed to be very small. The results of the numerical simulation are compared with known experimental and theoretical results. The hydrodynamic simulation shows characteristic intermittent pulsations of the drag and lift force on the cylinder. At $Re = 200$ a mix of secondary spanwise three-dimensional instabilities (A and B mode, rib vortices) could be observed. The spanwise wavelength of the rib vortices was found to be about 2–3 cylinder side lengths in the near wake. At $Re = 250$ the flow appears more organized showing a regular B mode pattern and a spanwise wavelength of about 1 cylinder side length. With an applied magnetic field a quasi-two-dimensional flow can be obtained at low $N \approx 1$ due to the strong non-isotropic character of the electromagnetic forces. The remaining vortices have their axes aligned with the magnetic field. With increasing magnetic fields these vortices are further damped due to Hartmann braking. The result that the 'quasi-two-dimensional' vortices have a curvature in the direction of the magnetic field can be explained by means of an asymptotic analysis of the governing equations. With very high magnetic fields the time-dependent vortex shedding can be almost completely suppressed. By three-dimensional visualization it was possible to show characteristic paths of the electric current for this kind of flow, explaining the action of the Lorentz forces.

1. Introduction

The self-cooled liquid metal fusion blanket has been intensively investigated for application in fusion reactors (e.g. Malang 1988). A circulating highly conducting liquid metal is used as coolant and breeder material. The interaction of this moving liquid conductor and the magnetic field confining the plasma has to be analysed

https://doi.org/10.1017/S0022112000001300 Published online by Cambridge University Press

carefully in order to keep the temperatures at the plasma facing the first wall within acceptable limits. The practical motivation for the present work stems from the fact that the flow of liquid metal coolant in the presence of the reactor's magnetic field system is likely to be laminar, whereas the need for high heat-transfer rates favours a turbulent or at least a time-dependent flow.

The induced electric currents in the fluid interact with the magnetic field and generate Lorentz forces which greatly change the flow patterns. For the strong magnetic fields applied in fusion reactors inertial forces are unimportant for many applications in the internal region of the flow. The Lorentz forces are mainly balanced by the pressure forces. The viscous effects are confined to thin boundary layers at the walls. Strong magnetic fields justify an asymptotic approach for calculating stationary, inertialess and laminar liquid metal MHD flow. This was done by, among others, Hunt & Ludford (1968), Bühler (1995) and Molokov & Bühler (1994) for various three-dimensional geometries. The calculated velocity fields and the pressure drop agree with the experiments but heat transfer calculations based on laminar inertialess flow show that an enhancement of heat removal as in turbulent hydrodynamic flows would be desirable. Experiments (Burr *et al.* 2000) and numerical simulations (Bühler 1996) demonstrated that persistent velocity fluctuations or time-dependent mixing are possible in such flows.

The evolution of turbulent flow under the influence of a magnetic field has been the subject of several theoretical (e.g. Sommeria & Moreau 1982; Davidson 1995) and experimental (e.g. Kolesnikov & Tsinober 1972*b*; Andreev & Kolesnikov 1997; Lahjomri, Caperan & Alemany 1993; Alboussière, Upenski & Moreau 1999) studies. As Joule dissipation is highly anisotropic, velocity components with non-zero gradient in the direction of the magnetic field are dissipated and vortical structures are elongated in this direction. This process can be described as propagation of momentum and vorticity along magnetic field lines. As a result vortices perpendicular to the magnetic field axis are dissipated rapidly whereas vortices aligned with the magnetic field are damped only weakly. MHD effects may even intensify vortices which have their axes parallel to the magnetic field ('reversed energy cascade' see e.g. Sommeria & Moreau 1982). As a result a quasi-two-dimensional flow evolves, which is three-dimensional only in the boundary layers.

Beside other possibilities described in Bühler (1996) or Burr *et al.* (2000) an obvious way to produce vortices in a insulated channel is through cylindrical obstacles, so-called turbulence promoters, which are aligned with the magnetic field. This concept has been investigated experimentally by Kit, Turuntaev & Tsinober (1970) and Kolesnikov & Tsinober (1972*b*). In the experiment of Kolesnikov & Tsinober (1972*a*) it was shown that in a strong magnetic field the axes of the vortices behind a grid were aligned with the magnetic field. Recent experimental results for a single insulated cylinder in an insulated duct are given in Frank, Barleon & Müller (2000) showing a linear dependence of the Hartmann number on the critical Reynolds number ($Re_c = 0.94 \pm 0.03 * M$) for the onset of time-dependent vortex shedding. It was also shown that the shedding frequency does not change substantially with a rising Hartmann number. The wake created by the cylinder is narrowed by the influence of the magnetic field. By means of an array probe for measuring the potential at the Hartmann walls it was possible to visualize indirectly the vortices shed by the cylinder. Earlier experiments showing qualitatively similar results were done by Papailiou (1984). Although his experiments were carried out in an open channel without a second Hartmann wall he also described the substantial change of the wake geometry under a magnetic field. For a conducting cylinder in an insulated

https://doi.org/10.1017/S0022112000001300 Published online by Cambridge University Press

duct see Andreev & Kolesnikov (1997). A review of other arrangements of the cylinder and the magnetic field is given in Lahjomri *et al.* (1993).

Although there are numerous theoretical and experimental studies, only a few somewhat complicated three-dimensional MHD channel flows, such as bend flows or flows in parallel channels, have been investigated by direct three-dimensional numerical simulations (e.g. Sterl 1990; Lenhart 1994; Leboucher 1999). A fully numerical approach is difficult because of the very thin boundary layers developing along the channel walls. The flow structure is governed by the currents in these boundary layers for the case of insulating walls. Resolving these boundary layers immediately leads to problems with storage and computing time. A large-eddy simulation (LES) of a turbulent channel flow under a uniform magnetic field was described in Shimomura (1991). Three-dimensional simulations of an MHD flows around obstacles are scarce. In Mutschke *et al.* (1997) a three-dimensional simulation of an MHD flow behind a cylindrical obstacle is described with the magnetic field aligned with the flow.

The problem considered in the present paper is an MHD flow around an insulated square cylinder placed in an insulated rectangular channel. The flow is exposed to a uniform magnetic field which is oriented perpendicular to two duct walls and aligned with the non-conducting cylinder. The aim is to show and explain the transition from an initial three-dimensional hydrodynamic flow to a quasi-two-dimensional MHD flow by the application of a magnetic field and the further damping of two-dimensional vortices by Hartmann braking. Three-dimensional visualizations of the vorticity are used to show the changes in the flow. Asymptotic methods are applied to explain observed effects. In addition the three-dimensional electric currents are visualized since knowledge of the paths of the currents makes it possible to explain the flow structure.

It should be noted that even hydrodynamic three-dimensional numerical simulations of the flow around a square cylinder, here used as initial flow for the application of a magnetic field, are quite rare in the literature for moderate Reynolds numbers ($Re = 150$–500). The first simulation was done by Sohankar, Norberg & Davidson (1999). In the present work, beside the basic properties, we also provide three-dimensional contours of the vorticity.

The formulation of the problem is given in the next section. In the §§ 3–5 the numerical methods, boundary conditions and the choice of the numerical grid are described. The results for the hydrodynamic case are described in § 6, the results for the MHD case in § 7. In § 8 the influence of weak inertial effects in a quasi-two-dimensional MHD flow is outlined. Finally the conclusions are provided in § 9.

2. Formulation

We consider the flow of an electrically conducting incompressible viscous Newtonian fluid (e.g. liquid metal). Under fusion blanket conditions the induced magnetic field is negligible compared to the imposed magnetic field because the magnetic Reynolds number $R_m = \mu\sigma v_0 a$ is very small ($R_m \ll 1$). In this case the isothermal flow is governed by the inductionless equations for the conservation of mass, momentum and charge:

$$\frac{\partial \boldsymbol{v}}{\partial t} + (\boldsymbol{v}\cdot\nabla)\boldsymbol{v} = -\nabla p + \frac{1}{Re}\Delta\boldsymbol{v} + N(\boldsymbol{j}\times\boldsymbol{e}_y), \tag{2.1}$$

$$\nabla\cdot\boldsymbol{v} = 0, \tag{2.2}$$

$$\nabla\cdot\boldsymbol{j} = 0, \tag{2.3}$$

https://doi.org/10.1017/S0022112000001300 Published online by Cambridge University Press

and by Ohm's law

$$\boldsymbol{j} = -\nabla\Phi + \boldsymbol{v} \times \boldsymbol{e}_y. \tag{2.4}$$

With the solenoidal current field (2.3) and (2.4) one can derive a Poisson equation for the electric potential:

$$\Delta\Phi = \nabla \cdot (\boldsymbol{v} \times \boldsymbol{e}_y), \tag{2.5}$$

which is more convenient to use for numerical calculations than Ohm's law (2.4). Here the variables $\boldsymbol{v} = (u, v, w)$, $\boldsymbol{j} = (j_x, j_y, j_z)$, p, t and Φ are the dimensionless velocity, electric current density, pressure, time and electric potential. They are normalized by the characteristic velocity in the duct: v_0, $\sigma v_0 B_0$, ρv_0^2, D/v_0 and $D v_0 B_0$. The material properties σ and ρ are the electric conductivity and the density of the fluid. The side length D of the square cylinder is chosen as the characteristic length scale of the problem. It should be noted that in MHD channel flows without internal obstacles the half-height a of the duct (here $a = 5D$) is commonly used as characteristic length scale. B_0 is the magnitude of the uniform and constant magnetic field $B\boldsymbol{e}_y$. Two independent dimensionless parameters appear. The Reynolds number

$$Re = \frac{v_0 D}{\nu} \tag{2.6}$$

denotes the ratio of inertia and viscous forces where ν is the kinematic viscosity. The interaction parameter

$$N = \frac{D\sigma B^2}{\rho\nu}, \tag{2.7}$$

also known as the Stuart number, represents a ratio of electrodynamic forces and inertia forces. A further non-dimensional group is the Hartmann number

$$M = DB\sqrt{\frac{\sigma}{\rho\nu}}, \tag{2.8}$$

which appears as the product $\sqrt{NRe}$. The square of the Hartmann number represents the ratio of electrodynamic forces and viscous forces. In addition to the governing equations, boundary conditions have to be specified which are discussed in §4. To describe the vortex shedding at the cylinder the Strouhal number is used:

$$St = \frac{fD}{v_0}, \tag{2.9}$$

where f is the shedding frequency. The oscillating lift and drag forces on the cylinder are scaled by the dynamic pressure $\frac{1}{2}\rho v_0^2 A_\perp$, where $A_\perp (A_\parallel)$ is the area of the cylinder perpendicular (parallel) to the main flow direction. In the present work only the pressure parts of the lift and drag forces were considered:

$$C_L = \frac{2}{A_\parallel}\int_{A_\parallel} p\,\mathrm{d}A, \qquad C_D = \frac{2}{A_\perp}\int_{A_\perp} p\,\mathrm{d}A. \tag{2.10}$$

3. Numerical methods

The system of equations (2.1)–(2.5) is solved by a finite difference method on an orthogonal equidistant grid. The spatial discretization is done on a staggered grid. All vector quantities are defined on the corresponding surfaces of the cell, while the scalar quantities are defined at the centre of the cell. The discretization is of second-order accuracy in time and space. The time is discretized by an explicit Adams–Bashforth

https://doi.org/10.1017/S0022112000001300 Published online by Cambridge University Press

scheme. Centred differences are used for the discretization of the diffusive term. For the convective terms a variant of the LECUSSO discretization scheme proposed by Günther (1992) is used. The basic algorithm requires the solution of two Poisson-type equations at each time step. The equation for pressure is derived from the fractional-step method (Kim & Moin 1985; Perot 1993). For the potential, equation (2.5) is solved.

In the fractional-step method for the pressure–velocity coupling equation (2.1) is integrated without the pressure term, resulting in a temporary velocity $\boldsymbol{v}'$. The pressure $p^{(n+1)}$, the superscript denoting the time step, is calculated to ensure a solenoidal velocity field, leading to

$$\Delta p^{(n+1)} = \frac{1}{\Delta t} \nabla \cdot \boldsymbol{v}', \tag{3.1}$$

where Δt is the time increment. Then $p^{(n+1)}$ is used to update $\boldsymbol{v}'$ to get the final $\boldsymbol{v}^{(n+1)}$:

$$\boldsymbol{v}^{(n+1)} = \boldsymbol{v}' - \Delta t \cdot \nabla p^{(n+1)}, \tag{3.2}$$

which is divergence-free. Knowing the new velocities $\boldsymbol{v}^{(n+1)}$ the electric potential and finally the currents are computed according to equations (2.5), (2.4). The currents are also divergence-free by construction.

The Poisson-type equations are solved by a direct method based on fast Fourier transforms (FFT) which are the fastest algorithms for the solution of the discrete Poisson equation in rectangular domains on orthogonal equidistant grids, see e.g. Botta *et al.* (1997). For more complicated domains with internal boundaries and obstacles as in this work the capacitance matrix method (e.g. O'Leary & Widlund 1979) provides a technique with the advantage of extending the use of fast Poisson solvers to more generally bounded regions. In this technique each of the Poisson equations for pressure and potential must be solved two times at every time step. The additional computational effort for the capacitance matrix method including the additional solution of two Poisson equations is easily compensated by the advantage of using a fast Poisson solver instead of taking another direct solver for an irregular geometry.

4. Boundary conditions

4.1. *Conducting walls*

The computation of the electric potential in arbitrary conducting walls requires the solution of the thin-wall condition (Walker 1981):

$$\boldsymbol{j} \cdot \boldsymbol{n} = -\nabla_t \cdot \left(\frac{\sigma_w}{\sigma} t_w \nabla_t \Phi \right). \tag{4.1}$$

Equation (4.1) expresses the conservation of charge at the fluid/wall interface. It is assumed that the thickness of the conducting wall is much smaller than the characteristic scale chosen earlier. With that assumption the electric potential over the thickness of the wall is nearly uniform. The currents leaving the fluid region enter the wall of non-dimensional thickness t_w and turn in the tangential direction producing a tangential potential distribution as stated in (4.1). The product $c = \sigma_w t_w / \sigma$ is referred to as the wall conductance ratio. By replacing the normal current at the fluid/wall interface by $\nabla \phi_n$ we finally get

$$\nabla \Phi_n = -\nabla_t \cdot (c \nabla_t \Phi). \tag{4.2}$$

https://doi.org/10.1017/S0022112000001300 Published online by Cambridge University Press

To ensure that the three-dimensional Poisson equation for the electric potential (2.5) matches the conservation law (4.2) an iterative method described by Leboucher (1999) is used.

4.2. *Treatment of the Hartmann layer*

With a magnetic field applied to the duct flow thin boundary layers develop at the channel walls. At the walls parallel to the magnetic field the so-called side layers appear which have the thickness $\delta \sim 1/\sqrt{M}$. At the walls perpendicular to the magnetic field very thin Hartmann layers with thickness $\delta \sim 1/M$ appear. For high values of M the Hartmann layers are so thin that it becomes unfeasible to resolve them numerically with a code based on equidistant grid spacing. To overcome this problem the flow region is split into parts. One is the core, where viscous effects are negligible in comparison with the electromagnetic interaction. The core is surrounded by viscous Hartmann and side layers near the walls. In many references the core is treated separately and viscous corrections are added that are required for satisfying no slip at the walls and to obtain a uniformly valid solution. In the present work the numerical resolution is high enough that the side layers are resolved accurately so that there is no need for an analytical side layer model. However the much thinner Hartmann layers would cause problems during the numerical analysis. For that reason an analytical boundary layer model is used here to describe the viscous corrections near the Hartmann walls Hunt & Ludford (1968).

The essence of the Hartmann layer model is that the layers provide a new current path, in addition to that in the wall. This leads to a modification of the thin-wall condition which, in the form

$$\boldsymbol{n} \cdot \nabla \Phi = -\nabla_t \cdot ((c + \delta) \nabla_t \Phi) \tag{4.3}$$

is now applied to the core potential. Although this boundary condition was initially used for inertialess MHD flows at high Hartmann numbers it is also advantageous for inertial MHD flows as shown by Leboucher (1999) since it allows the Hartmann layers to be left unresolved by the numerical grid while at the same time considering the effects due to the closing together of the currents in the Hartmann layer and Hartmann wall. The numerical simulation is now only limited by the resolution of the side layers, which are much thicker than the Hartmann layers and easier to resolve. With the known core solution it is possible to reconstruct the solution in the Hartmann layers if desired.

If equation (4.3) is used as a boundary condition for the core flow at the Hartmann wall, the boundary conditions for the velocity also have to be modified. This together with the boundary conditions for the electric potential at the entry and outlet is explained in the next section. The method is somewhat similar to that applied by Walker, Ludford & Hunt (1972), where the Hartmann layers are treated separately from a combined core–side layer solution for a steady-state three-dimensional expanding flow.

4.3. *Velocity, electric potential and pressure*

The sidewalls of the duct and the cylinder are impermeable and friction is present. So the boundary condition for the velocity at the walls is

$$\boldsymbol{v}|_{wall} = 0. \tag{4.4}$$

The solution of the boundary layer equations for the Hartmann layers results in an exponential decay of the tangential components of velocity from the value in the

https://doi.org/10.1017/S0022112000001300 Published online by Cambridge University Press

core to zero at the wall. Since the numerical calculations are performed for the core region including the side layers, appropriate conditions for the core velocity have to be specified at the Hartmann walls because no slip is already accounted for in the Hartmann layer model. A practical boundary condition here is

$$\frac{\partial^2 \boldsymbol{v}_t}{\partial y^2} = 0, \tag{4.5}$$

which corresponds to a linear extrapolation of the core solution towards the wall. This condition is in agreement with that given by Hunt & Ludford (1968) for core variables at large Re and N.

With the known exponential profile of the tangential velocity component in the Hartmann layer and the continuity equation a boundary condition for the normal velocity component of the core flow at the Hartmann wall can be derived (Hunt & Ludford 1968; Leboucher 1999):

$$\boldsymbol{v}_n = M^{-1} \nabla_t \cdot \boldsymbol{u}_t, \tag{4.6}$$

so that at leading order $\boldsymbol{v}_n = 0 + O(M^{-1})$. The error introduced by the boundary condition used, $\boldsymbol{v}_n = 0$, is $O(M^{-1})$ and vanishes for high Hartmann numbers. The normal component of the velocity becomes negligible since the layers are very thin for large M and do not carry significant volume flux compared with the core.

At the entry the flow profile is fixed at a fully developed MHD-flow profile which has to be computed beforehand. At the outflow, vortices produced at the cylinder are expected to leave the domain. This requires the use of non-reflective boundary conditions to minimize upstream effects from the outlet. In the present work a convective boundary condition was chosen (see e.g. Sani & Gresho 1994 or Sohankar *et al.* 1999):

$$\frac{\partial \boldsymbol{v}}{\partial t} + U \frac{\partial \boldsymbol{v}}{\partial x} = 0, \tag{4.7}$$

where U was set to the mean velocity at the entry.

The boundary conditions for the electric potential at the entry and the outlet of the computational domain are chosen such that no electric currents leave or enter the domain, to be compatible with the solenoidal current field:

$$\left.\frac{\partial \Phi}{\partial \boldsymbol{n}}\right|_{entry} = 0, \qquad \left.\frac{\partial \Phi}{\partial \boldsymbol{n}}\right|_{outlet} = (\boldsymbol{v} \times \boldsymbol{B}) \cdot \boldsymbol{n}. \tag{4.8}$$

This results in a zero normal component of the current at the entry and at the outlet. The outlet condition is not exact in the sense that it is valid only averaged across the exit plane. If it is applied locally as shown in equation (4.8) it is assumed that currents perpendicular to the exit plane are absent. This is not generally the case if vortices leave the computational domain. However these currents are on the order of M^{-1} and negligible for large M in comparison with the contributions taken into account.

All walls are treated as insulated. At the Hartmann walls the model boundary condition (4.3) for the potential was used with the wall conductivity $c = 0$. At the sidewalls the thin-wall condition (4.2) with $c = 0$ was used which results in a homogeneous Neumann boundary condition. At the insulated cylinder walls a homogeneous Neumann boundary condition was also used.

In the numerical algorithm described in § 3 a Poisson-type equation for the pressure (3.1) is solved. From equation (3.2) a boundary condition for the pressure can be

https://doi.org/10.1017/S0022112000001300 Published online by Cambridge University Press

derived:

$$\left.\frac{\partial p}{\partial \boldsymbol{n}}\right|_{boundary}^{n+1} = \frac{1}{\Delta t}(\boldsymbol{v}' - \boldsymbol{v}^{n+1}) \cdot \boldsymbol{n}. \tag{4.9}$$

Owing to the use of staggered grids for velocity and pressure, the pressure at the boundary is independent of the introduced temporary velocity at the boundary (see e.g. Peyret & Taylor 1983; Lenhart 1994). With the assumption that the boundary values for the temporary velocity $\boldsymbol{v}'$ are the same as for the velocity $\boldsymbol{v}^{n+1}$ a homogeneous Neumann boundary condition for the pressure can be deduced from equation (4.9). Therefore the pressure only needs to be calculated for interior mesh points.

4.4. *Boundary conditions for the hydrodynamic calculations*

The computed three-dimensional hydrodynamic results are intended for use as initial condition in the MHD case to investigate the damping of the vortices due to a magnetic field. Therefore the boundary conditions were chosen to ensure minimal entry effects for MHD calculations. At the entry a uniform block profile was used which is quite similar to the flow profile of a fully developed MHD flow in an insulated duct. At the sidewalls the no-slip condition was used. The choice of this boundary condition for the hydrodynamic case may influence the vortex shedding due to the additional blockage effect of the developing boundary layers at the sidewalls ($\pm z$) which confine the flow. This was necessary because in the MHD case the side layers are resolved by the numerical grid.

At the bottom and top wall, where in the MHD case the thin Hartmann layers are located, a Neumann-type boundary condition has been adopted for the u- and w-components of the velocity and a Dirichlet-type boundary condition for the v-component:

$$\frac{\partial u}{\partial y} = 0, \quad \frac{\partial w}{\partial y} = 0, \quad v = 0. \tag{4.10}$$

This boundary condition is compatible with the model for the Hartmann layer used later in the MHD case. The drawback of this boundary condition compared to an undisturbed hydrodynamic computation near the wall is the zero normal component of the velocity, which may influence vortices near the wall. For purely hydrodynamic computations homogeneous Neumann conditions should also be used for the v-velocity as in Persillon & Braza (1998). Additionally it should be noticed that periodic boundary conditions in the spanwise direction are questionable for hydrodynamic simulations since in many experiments skewed vortex shedding can be observed and the flow does not show periodic properties. At the outlet the convective boundary condition (4.7) already mentioned was used.

5. Numerical grid resolution

The flow configuration is known to be very sensitive to various numerical and physical parameters. Extensive testing of the influence of numerous parameters like grid resolution, domain size, blockage, boundary conditions, far- and near-body resolution for the square cylinder was done by Sohankar, Norberg & Davidson (1997, 1998). It appears that even recent two-dimensional simulations of this case are not independent of the grid, but they are believed to be good enough to show influences of physical parameters.

The present application justifies the use of orthogonal equidistant grids. The main purpose of the computation was to investigate the downstream behaviour of the

https://doi.org/10.1017/S0022112000001300 Published online by Cambridge University Press

Case	*Re*	Grid $n_x \times n_y \times n_z$	Points	Min grid size
1	200	$200 \times 80 \times 100$	1.6×10^6	0.1
2	250	$250 \times 80 \times 125$	2.5×10^6	0.08

TABLE 1. Grid parameters for the two cases investigated.

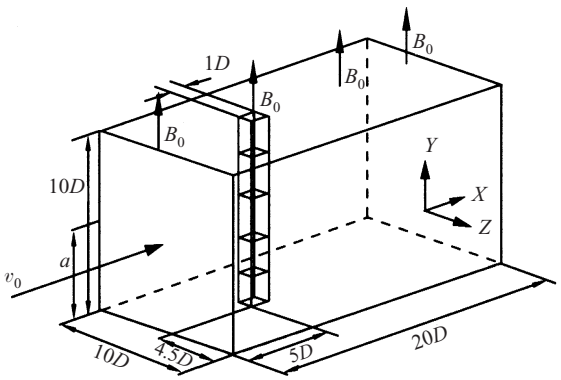


FIGURE 1. Geometry and coordinates.

vortices shed in the presence of a magnetic field. Consequently a coarser grid in the wake of the cylinder, as it is often used in purely hydrodynamic flows, is not applicable because additional numerical diffusion may dominate over the MHD damping. The best compromise with respect to the available computer resources and solvers was to use an equidistant grid with the drawback of lower resolution of the boundary layers at the cylinder. After some two-dimensional tests it was found that the resolution of the boundary layers should be at least 3–4 grid points to get reasonable results. This could be achieved by the two- and three-dimensional versions of the equidistant grids used in this work (see table 1). The solid blockage in the geometry used (see figure 1) was 10%. The number of nodes distributed over one unit length of the cylinder in the (x, z)-plane was 10 in case 1 and 13 in case 2. The distance between the nearest grid point and the cylinder surface was $\delta = 0.05$ for case 1 and $\delta = 0.04$ for case 2. The geometry and grid resolution used for the two-dimensional hydrodynamic case is found to have two main effects on the results. Due to the high blockage the computed values for the mean drag coefficient ($C_D = 1.75$) were higher than in other recent simulations with low blockage. The lift coefficient is very sensitive to various numerical parameters. In the present simulation the lift coefficient is sensitive to the grid resolution near the obstacle and falls with a coarser grid resolution, which might explain the low values of the RMS lift coefficient $C_L = 0.192$ in the present two-dimensional simulation. These effects of the blockage ratio and grid resolution were also reported by Sohankar *et al.* (1997, 1998). It should be noted that better agreement could be found with the calculations of Davis, Moore & Purtell (1984) who used a blockage ratio of 16% and a comparable grid resolution.

The Strouhal number for the two-dimensional case was found to be $St = 0.166$ which is in the range of values $St = 0.165$–0.170 found by the latest simulations of Sohankar (1998) for two-dimensional calculation of the square cylinder for various blockage and grid resolution parameters. It is close to the value of $St = 0.16$ found by Minewitsch, Franke & Rodi (1994) at a blockage ratio of 8.3%. The reason why

https://doi.org/10.1017/S0022112000001300 Published online by Cambridge University Press

despite the low boundary-layer resolution near the obstacle the Strouhal number agrees quite well with the existing results may lie in the fact that the resolution of the absolutely unstable area behind the cylinder is more important. This can be achieved with comparatively coarse grids. Following Huerre & Monkewitz (1990), there is a strong evidence that the explanation of von Kármán vortex shedding cannot be found in the details of flow separation from the cylinder surface. From stability analysis of the wakes behind blunt bodies it is known that the key to the frequency selection of vortex shedding behind blunt bodies is a hydro-mechanical resonance mechanism in the absolutely unstable area, see also Oertel (1990).

From this it may be concluded that if one is interested in the transient and the qualitative spatial evolution of the flow, the resolution in the (x, z)-plane of the grid used here is sufficient. It is now possible to place enough grid points along the spanwise direction for the three-dimensional calculation to resolve the expected streamwise vortices with a wavelength of approximately D with respect to the available computer resources. In Zhang, Noack & Eckelmann (1994) a systematic grid variation was carried out for the circular cylinder to find the lowest allowable grid resolution in the spanwise direction for one wavelength of the streamwise vortices, i.e. two counter-rotating streamwise vortices. Following their recommendation we use ~ 8 grid points for the resolution of one wavelength. The spanwise distance ($10D$) was chosen to be as long as possible in order to avoid the inhibition of possible instability modes and their interactions.

6. Results for the hydrodynamic case

As the main objective of this work was the investigation of MHD flow, the hydrodynamic part was reduced to the calculation of the basic flow patterns and properties of the flow. To the knowledge of the authors, only one published numerical simulation of the three-dimensional case exists, by Sohankar *et al.* (1999). Up to now no three-dimensional visualization of the flow has been published. Therefore the present results for the hydrodynamic case are reported. As a first example the flow at a Reynolds number of 200 based on the cylinder side length is investigated. In the hydrodynamic case the Kármán vortex street evolves with secondary instabilities forming three-dimensional streamwise vortex structures (see figure 3). These are similar to those behind a circular cylinder investigated by Williamson (1996) at the same Reynolds number. The present simulation of the three-dimensional hydrodynamic velocity field is later used as initial condition for the simulation with an applied magnetic field.

The flow field was discretized according to case 1 (table 1). The dimensionless time step was set to 2×10^{-3} which fulfils the stability limits for the Adams–Bashforth scheme used in combination with the LECUSSO Upwind-scheme by Günther (1992), see Mück (1999). The initial condition is equivalent to an impulsive start of the flow with the velocity v_0 everywhere in the flow field.

The dimensionless drag and lift coefficients C_D, C_L are computed at every time step. The Strouhal number was determined from the frequency f of the fluctuating lift signal when the vortex shedding was established.

In the present calculation the two- and three-dimensional vortex shedding is generated without imposing external perturbations. The self-excitation is due to truncation errors and round-off errors of the computer. After a temporary two-dimensional state the flow develops self excited three-dimensional flow patterns (see figure 3). The flow transition from the temporary two-dimensional state to the three-dimensional state is

https://doi.org/10.1017/S0022112000001300 Published online by Cambridge University Press

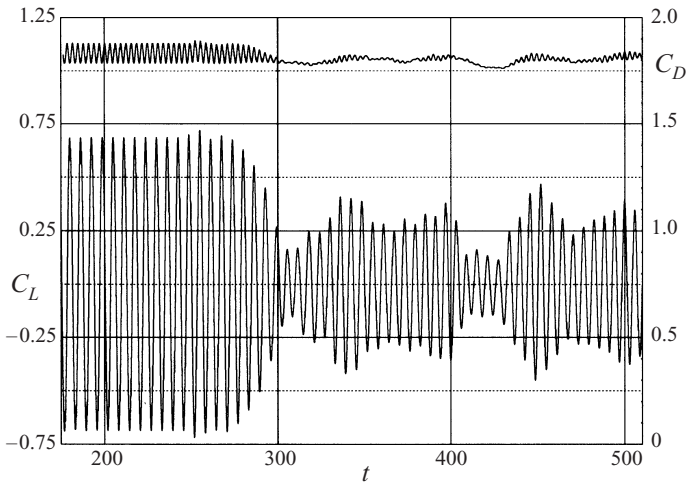


FIGURE 2. Plot of the lift and drag forces on the cylinder at $Re = 200$.

marked by a sudden decrease in the lift and drag force at $t \approx 290$, see figure 2. The Strouhal number in the two-dimensional state ($St = 0.166$) is slightly higher than in the following three-dimensional state. The beginning of the transition is marked by slight disturbances of the lift and drag force amplitude.

Compared to the simulation of Sohankar *et al.* (1999) at the same Reynolds number, in the present simulation the transition to the three-dimensional state is delayed. However the transient behaviour in the two- and three-dimensional state of the flow agrees well.

The flow exhibits characteristic force pulsations with distinct regions of high and low values of the drag and lift coefficient (see figure 2). The apparent random pulsations have a repetition time of roughly 60–80 time units (10–13 shedding periods).

Following Zhang *et al.* (1994) the second wake instability in the case of the circular cylinder is a Taylor or Görtler instability forming rib-like vortices. The same mechanism may be present in the near wake of the square cylinder because of the similar flow patterns.

In the present simulation at the aspect ratio used of 10 a mix of spanwise three-dimensional instabilities with substantial deformation of the primary instability was observed. This makes the determination of the spanwise wavelength and the type of the secondary instability (mode A, mode B) difficult. The spanwise wavelength of the rib vortices is found to be approximately $2D$–$3D$ in the near wake one diameter downstream of the cylinder. Further downstream the spanwise wavelength is increasing. The flow shows ingredients of spanwise secondary mode A and B instability structures. Also vortex-adhesion points at the cylinder could be observed.

One reason for the irregular secondary vortices could be a competition between modes, in analogy to the circular cylinder. In a stability analysis of Barkley & Henderson (1996) for the circular cylinder it is shown that there are several unstable mode A wavelengths above a Reynolds number of 190. For a sufficiently high aspect ratio it is expected that the different modes alternate in time and space. Therefore irregular flow patterns are expected, see e.g. Henderson (1997) for the circular cylinder. For $Re = 250$ a type of secondary instability similar to the mode B instability for the circular cylinder flow is found. The grid resolution was enhanced to 2.5×10^6 grid points corresponding to case 2 in table 1. The flow pattern observed is more regular

https://doi.org/10.1017/S0022112000001300 Published online by Cambridge University Press

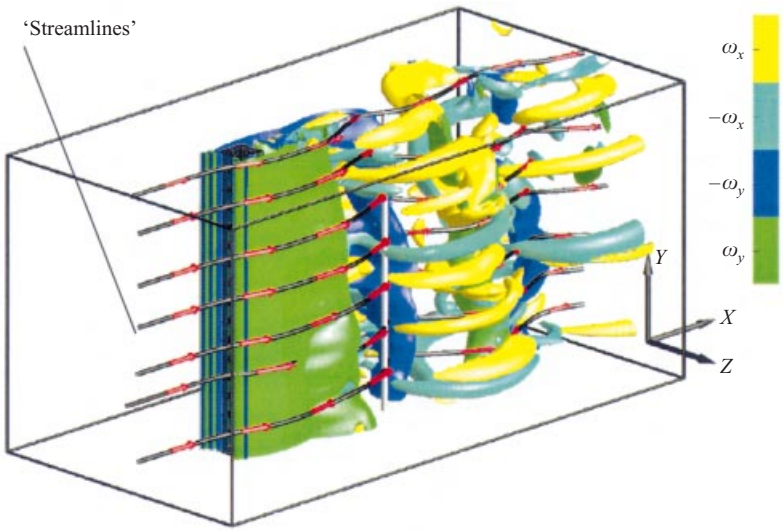


FIGURE 3. Isovorticity surface plot of the three-dimensional hydrodynamic flow around a square cylinder at $Re = 200$, $\omega_y = \pm 6$; $\omega_x = \pm 3$.

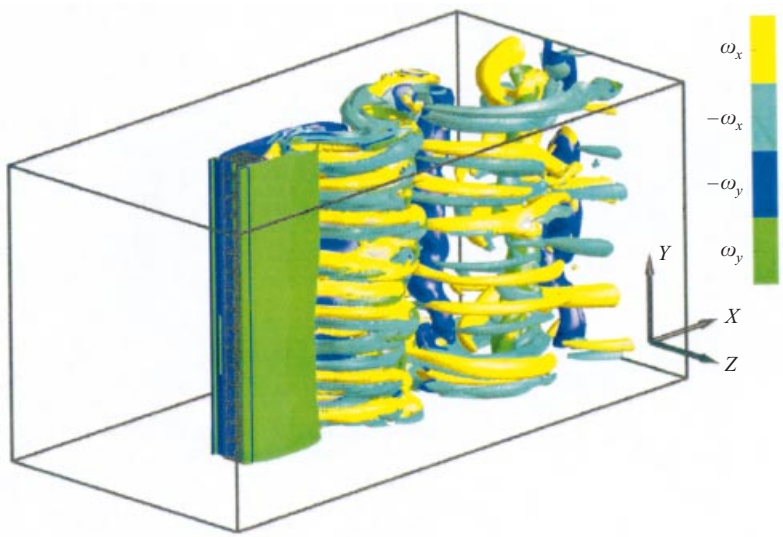


FIGURE 4. Hydrodynamic flow, Mode B vortex shedding $Re = 250$; $\omega_y = \pm 6$; $\omega_x = \pm 3$.

than in the case of $Re = 200$ (see figure 4). It appears that the spanwise wavelength of the streamwise vortices now is $\sim 1D$. Comparing figure 4 with the visualizations of Zhang *et al.* (1994) for the mode B shedding from the circular cylinder at $Re = 260$ shows an obvious similarity. From the visualizations it can be also observed that the streamwise vortices are in an inline arrangement which marks mode B vortex shedding following Williamson (1996). The drag and lift forces show a similar behaviour to the case $Re = 200$. Although not monitored over a sufficiently long time due to resource limitations there was a tendency for the force pulsations to occur less frequently than in the case $Re = 200$.

https://doi.org/10.1017/S0022112000001300 Published online by Cambridge University Press

With regard to the grid resolution used, the blockage effects and the sensitivity to various numerical parameters the present hydrodynamic simulation seem to be in acceptable agreement with previous results for the hydrodynamic case reported in Sohankar *et al.* (1999).

7. Results for the magnetohydrodynamic case

7.1. *Transition towards two-dimensional flow*

The result for the hydrodynamic case (see previous section) is used as initial condition for the MHD case. The same grid resolution as in the hydrodynamic case was used to avoid different numerical dissipation. Especially at low interaction parameters the flow may have three-dimensional components before it becomes two-dimensional at higher interaction parameters. Additional boundary conditions for the electric potential are specified according to § 4.

The first case investigated was at $Re = 200$, $M = 6.33$, $N = 0.2$. These values correspond to a rescaled Hartmann number $Ha = 31.6$ and an interaction parameter $N_{\|} = 1$. The groups $Ha = \alpha M$ and $N_{\|} = \alpha N$ are based on the Hartmann length a as used in duct flow problems. The aspect ratio α is denoted by $\alpha = a/D = 5$.

The result is shown in figure 5. Although at these parameters the magnetic field can be considered as weak (compared to fusion-relevant parameters) the action of the magnetic field on the streamwise vortices is quite obvious. These vortices, which are perpendicular to the magnetic field, are damped strongly. At locations where due to the curvature of the primary Kármán vortices vorticity components perpendicular to the magnetic field appear, strong damping also occurs resulting in a fragmentation of the vortices into two parts further downstream (see the arrows in figure 5). Diffusion of vorticity in the direction of the magnetic field further downstream, which leads to an elongation of the remaining vortex fragments, could not be observed because the channel was too short. A further interesting detail regarding figure 5 is that the eddies have their ends perpendicular to the wall to a good approximation. Following the analysis of Sommeria & Moreau (1982) for high Hartmann numbers and interaction parameters the electric boundary conditions at an insulating wall can be transformed into a single condition for the vorticity which requires that

$$\frac{\partial v_{\perp}}{\partial y}(x, 0, z, t) = O\left(\frac{v_0}{M l_{\perp}}\right) = O\left(\frac{v_0}{\sqrt{Re}\quad l_{\|}}\right), \tag{7.1}$$

where $v_{\perp}$ is the velocity component perpendicular to the magnetic field, i.e. parallel to the Hartmann wall, and $l_{\perp}$ and $l_{\|}$ are typical length scales perpendicular and parallel to the magnetic field. The physical interpretation of the order of magnitude in equation (7.1) is that the vortices have their ends perpendicular to the Hartmann wall although they could bend in the bulk of the flow. It is remarkable that this characteristic property of the MHD flow can already be observed in figure 5 at comparatively low Hartmann numbers and interaction parameters. The tendency towards an alignment in the magnetic field direction is already visible.

The next calculation at $M = 14.2$ ($Ha = 71$) and $N = 1$ ($N_{\|} = 5$) was started using the previous computation at $Re = 200$, $M = 6.33$, $N = 0.2$ as initial value. Since for this case the inertia forces have the same magnitude as the electrodynamic forces ($N = 1$) there should be a strong tendency towards a two-dimensional flow, i.e. an alignment of the vortices in the magnetic field direction and a complete damping of vorticity components perpendicular to the magnetic field. This can be clearly observed

https://doi.org/10.1017/S0022112000001300 Published online by Cambridge University Press

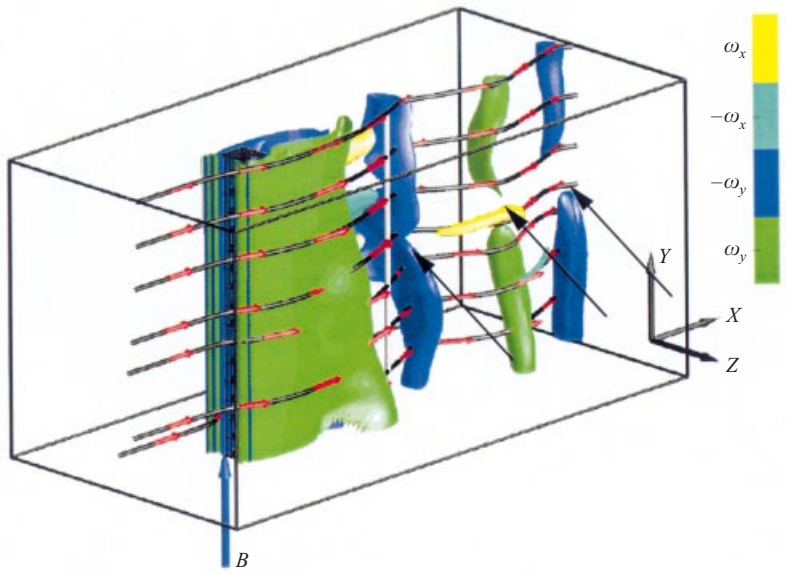


FIGURE 5. Isovorticity surface plot at $Re = 200$, $M = 6.33$, $N = 0.2$, $\omega_y = \pm 6$; $\omega_x = \pm 3$.

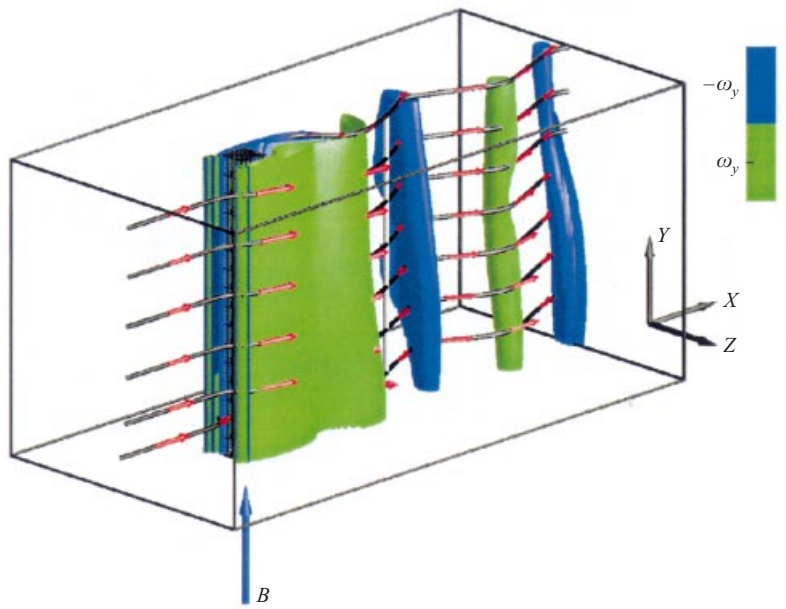


FIGURE 6. Isovorticity surface plot at $Re = 200$, $M = 14.2$, $N = 1$, $\omega_y = \pm 6$; surfaces $\omega_x = \pm 3$ are not present.

in figure 6 although the simulation time was not long enough to reach the end of the transition. For reasons of computer time and costs the simulation was stopped when the differences in successive periods became small.

To observe the transition to two-dimensionality one can consider the y-component of the velocity parallel to the magnetic field at fixed parameters. In figure 7 the transient behaviour of the velocity parallel to the magnetic field is shown at three

https://doi.org/10.1017/S0022112000001300 Published online by Cambridge University Press

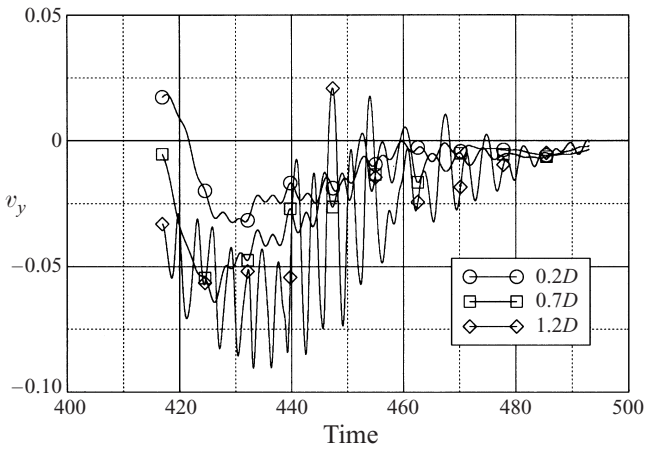


FIGURE 7. $Re = 200$; $M = 14.2$; $N = 1$: transient behaviour of v_y in the mid-plane at three different locations in the wake of the cylinder.

different monitoring locations in the midplane ($y = 5$) of the duct in the wake of the cylinder. It can clearly be seen that the fluctuations and the value of the y-component of velocity tend to zero. From this it can be concluded that the transition to the two-dimensional state occurs in the interval $0.2 \leqslant N \lesssim 1$.

During the transition to a two-dimensional state the flow is shaped in such a way that the interaction with the magnetic field is reduced to a minimum. The flow evolves so as to minimize the global Joule dissipation. The electric currents in a perfectly two-dimensional flow would vanish (no Joule dissipation) assuming that the flow domain is infinite without Hartmann walls. Without electric currents there is no coupling between the magnetic field and the flow, i.e. the flow is hydrodynamic. This may be also concluded from the rotation of Ohm's law (eq. (2.4)) where the currents vanish when the flow is two-dimensional.

In the present case with Hartmann walls the flow achieves a quasi-two-dimensional state (with minimized global Joule dissipation) which is three-dimensional only in the very thin viscous Hartmann layers. The currents close together in the Hartmann layers and cause a continuous weak damping of the two-dimensional vortices in the core (Hartmann damping). Disregarding the Hartmann damping, which acts on a larger time scale than the Lorentz force, the development follows the general principles noted in Davidson (1995). The Lorentz force acts to redistribute angular momentum in the magnetic field direction. The component of the angular momentum parallel to the magnetic field is preserved. The orientation of the axis of the cylinder parallel to the magnetic field facilitates the generation of two-dimensional flow structures since the main Kármán vortices are aligned with the magnetic field. The transition of the flow to a two-dimensional structure is achieved due to the suppression of the secondary instability of the vortex street by the magnetic field as described in § 6. Beyond a specific threshold of the magnetic field the three-dimensional patterns completely disappear. In the following a rough estimate is given for the time scales of the transition to a two-dimensional state for low magnetic Reynolds numbers in an unbounded domain. As already stated in Sommeria & Moreau (1982) the vorticity in the magnetic field direction satisfies

$$\frac{\partial \boldsymbol{\omega}_y}{\partial t} = \frac{1}{Re}\Delta_\perp \boldsymbol{\omega}_y - N\Delta_\perp^{-1}\frac{\partial^2 \boldsymbol{\omega}_y}{\partial y^2}, \tag{7.2}$$

https://doi.org/10.1017/S0022112000001300 Published online by Cambridge University Press

assuming that the flow is already close to two-dimensional with $\partial/\partial y \ll \partial/\partial x, \partial/\partial z$ and $v \lesssim u, w$ (neglecting classical vortex stretching). If the Reynolds number is large $Re \gg 1$ one may neglect the viscous part. The remainder of the right-hand side demonstrates the diffusive character of the propagation of disturbances due to electromagnetic forces. This pseudo-diffusion can be regarded as a degenerate form of Alfvén-wave propagation for small R_m. A typical time scale for the suppression of velocity differences between two transverse planes distance $l_\parallel$ apart can be derived from equation (7.2):

$$t_d \approx \frac{1}{N}\frac{l_\parallel^2}{l_\perp^2} = \tau\left(\frac{l_\parallel}{l_\perp}\right)^2, \tag{7.3}$$

where the magnetohydrodynamic interaction time τ is the typical time scale for the damping of isotropic turbulence. Velocity gradients in the magnetic field direction are suppressed, which results in an elongation of vortices in the magnetic field direction (magnetic vortex stretching). A flow will be two-dimensional if the time required for diffusion along field lines is shorter than a characteristic time in the problem, the latter being in the present case the inverse of the Strouhal number,

$$t_d \lesssim \frac{1}{St}. \tag{7.4}$$

Roughly speaking, a sufficient condition for a quasi-two-dimensional flow requires that

$$N \gtrsim a^2 St. \tag{7.5}$$

Since it is assumed that every perturbation must be diffused over the half-height a of the duct the relation gives larger interaction parameters than observed in the present case where the setup facilitates the transition to a two-dimensional flow.

It should be noted, although not proved in this work, that the two-dimensional transition should occur for all $Re > 200$ at the same interaction parameter since the ratio of electromagnetic and inertia forces, which is the important ratio for this process, should remain constant for the two-dimensional transition. As shown also in equation (7.2) the MHD vortex stretching effect, which causes the transition to a two-dimensional flow, is only dependent on the interaction parameter at high Reynolds numbers.

The only experiments known to the authors where the transition to a two-dimensional laminar flow in a comparable setup was investigated were those of Kit *et al.* (1970) and Kolesnikov & Tsinober (1972*b*). They investigated among other configurations the flow behind an insulated circular cylinder aligned with the magnetic field in an insulated channel with mercury. The Reynolds number was $Re \approx 8700$. At a critical interaction parameter $N \approx 1.2$ (based on the cylinder diameter) the flow was quasi-two-dimensional. This was indicated with a coefficient of three-dimensionality. Measurements of the fluctuations in a plane perpendicular to the magnetic field showed that due to the suppression of turbulent transport intensified generation of two-dimensional disturbances, with the axis parallel to the magnetic field, takes place. It was additionally observed that the critical interaction parameter did not depend on the Reynolds number.

These experimental results for the transition to a two-dimensional laminar flow in a comparable setup are in a good agreement with the present numerical calculation. Nevertheless the tendency towards a two-dimensional flow at $N \sim 1$ was also observed in completely different setups. In Zikanov & Thess (1998) the transformation of initially isotropic turbulence in a periodic box without walls was numerically investi-

https://doi.org/10.1017/S0022112000001300 Published online by Cambridge University Press

gated. In their case at $N \sim 1$ turbulent bursts alternate with periods of quasi-laminar, quasi-two-dimensional behaviour.

7.2. *Effects of Hartmann damping*

The following calculations show the damping of the two-dimensional laminar flow due to Hartmann damping, which is reflected in a decline of the vortex diameters as the (two-dimensional) vortices travel downstream. The main aim was to find the parameters where the vortex street is completely damped. During the calculations an additional effect on the vortices appeared, which was not shown in any previous MHD calculation. The vortices are rejuvenated at their ends where they touch the Hartmann walls. This weak effect of inertia is explained in § 8.

Sommeria & Moreau (1982) show that for quasi-two-dimensional MHD flows in insulated ducts the damping of two-dimensional vortices due to the closing of currents in the Hartmann layer acts on a time scale

$$\tau_{Ha} = \alpha \left(\frac{N}{M} \right)^{-1}. \tag{7.6}$$

As the Hartmann damping acts on a longer time scale than the MHD damping of isotropic turbulence (equation (7.3)) much higher interaction parameters are required to damp the vortex street completely. One can expect that, for the core when τ_{Ha} is smaller than a characteristic time scale of the problem, here $\tau_c = 1/St$, all time-dependent properties of the flow will undergo a fast transition towards a stationary solution. This reasoning leads to a complete damping of time-dependent motion when

$$\tau_{Ha} < \tau_c = 1/St, \tag{7.7}$$

or when

$$N > \alpha MSt. \tag{7.8}$$

The relation (7.8) is especially useful, since it provides a unique representation of results for different aspect ratios. This is helpful when different experiments or calculations are compared. Bühler (1996) gives an extension of equation (7.6) for quasi-two-dimensional MHD flows with thin conducting walls as

$$\tau^*_{Ha} = \alpha \left(\frac{N}{M} + \frac{c_{Ha} N}{1 + c_{Ha}} \right)^{-1}. \tag{7.9}$$

In the limit of non-conducting walls equation (7.6) is recovered. The dimensionless damping time τ^*_{Ha} is useful to compare the MHD damping of two-dimensional vortices in different geometries which produce vortices of different aspect ratio. Important for the MHD damping of vortices is their typical aspect ratio $\alpha = a/l_\perp$ ($l_\perp \approx D$). In spite of identical Hartmann number and interaction parameters, which are usually based on one typical length scale of the problem, the damping of vortices with a different aspect ratio is different. The MHD damping becomes weaker with higher aspect ratio. The next calculation at $M = 20$ ($Ha = 100$) and $N = 2$ ($N_\parallel = 10$) was started using the result of the previous computation at $Re = 200$, $M = 14.2$, $N = 1$ as initial value. In this case the electrodynamic forces are dominant and the flow becomes two-dimensional. This can be clearly seen in figure 8. The alignment of the shed vortices in the magnetic field direction is almost perfect. The flow is quasi-two-dimensional with the exception of the flow in the Hartmann layers. Additionally the weak damping of the two-dimensional vortices downstream due to the closure of the

https://doi.org/10.1017/S0022112000001300 Published online by Cambridge University Press

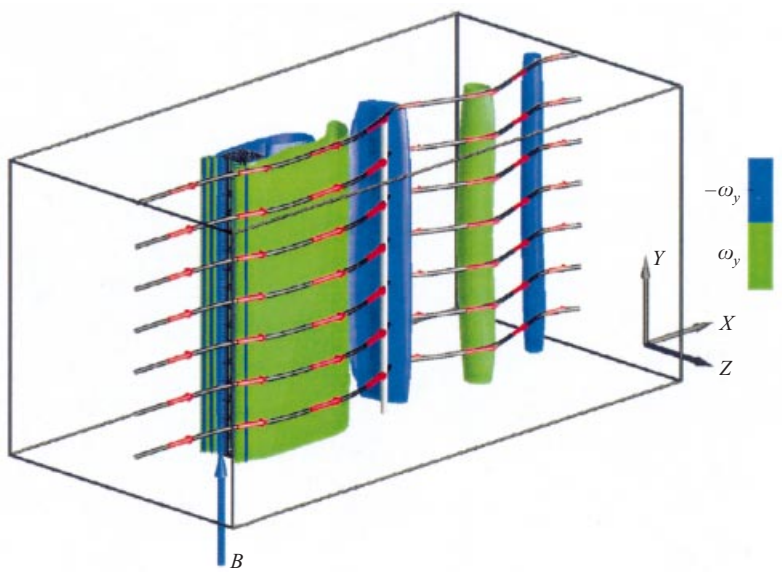


FIGURE 8. Isovorticity surface plot at $Re = 200$, $M = 20$, $N = 2$, $\omega_y = \pm 6$; surfaces $\omega_x = \pm 3$ are not present.

currents in the Hartmann layers can already be observed. The vortices decrease in diameter as they travel downstream.

At higher interaction parameters an additional effect besides the vortex damping becomes visible. Although the effect is rather weak it is obvious from figures 9 and 10 that the vortices are rejuvenated at their ends and look like cigars. This effect is also visible in the potential (see e.g. figure 11(*b*)) since the potential is linked to the stream function in quasi-two-dimensional flows, see e.g. Sommeria & Moreau (1982).

This result may have some importance for potential measurements in MHD flows where it is commonly assumed that the flow is strictly two-dimensional and the potential distribution is mapped to the Hartmann walls where it is measured by potential probes in the wall. Due to the curvature of the potential isolines along the direction of the magnetic field the potential distribution at the Hartmann wall tends to be equallized and the potential differences may fall below the precision of the measurement technique. In this case an existing vortex can no longer be detected by potential probes in the wall.

Interestingly, similar results for a potential variation in magnetic field direction have been obtained for laminar buoyant MHD flows in an asymptotic solution of Bühler (1998) where inertia has been neglected. This derivation can be modified by taking into account weak inertial effects to explain the curvature of the vortices. The analysis is presented in § 8.

In figures 10, 11(*a*) and 11(*b*) for the calculation at $M = 52.8$ ($Ha = 264.4$) and $N = 14$ ($N_\parallel = 70$) plots of vorticity and potential are shown. In figure 10 the stronger Hartmann damping compared to the previous cases can be seen. The vortices decrease rapidly in diameter as they travel downstream. The curvature of the vortices in the direction of the magnetic field is still visible. One vortex close to the exit seems to exist only in the core of the flow (figure 10). In this case the representation of a vortex by vorticity surfaces of a fixed level is misleading, since at a lower level of ω_y the vortex still exists over the full height between the Hartmann walls. The isoline plots

https://doi.org/10.1017/S0022112000001300 Published online by Cambridge University Press

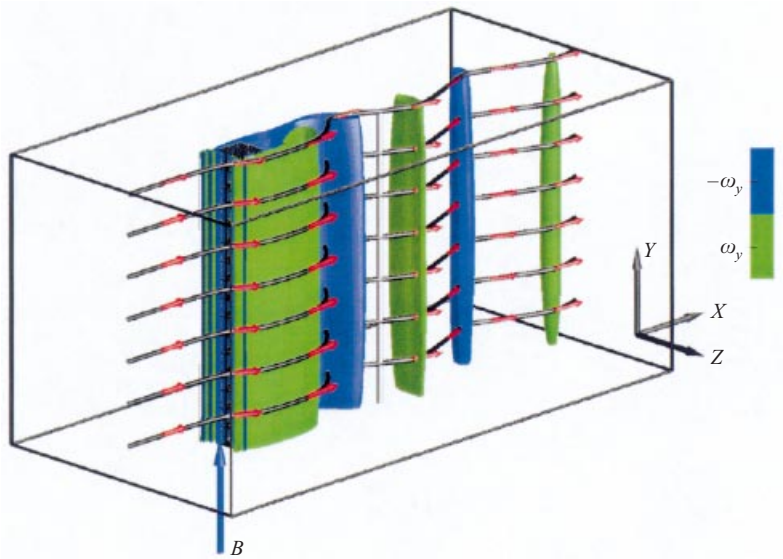


FIGURE 9. Isovorticity surface plot at $Re = 200$, $M = 28.3$, $N = 4$, $\omega_y = \pm 6$; surfaces $\omega_x = \pm 3$ are not present.

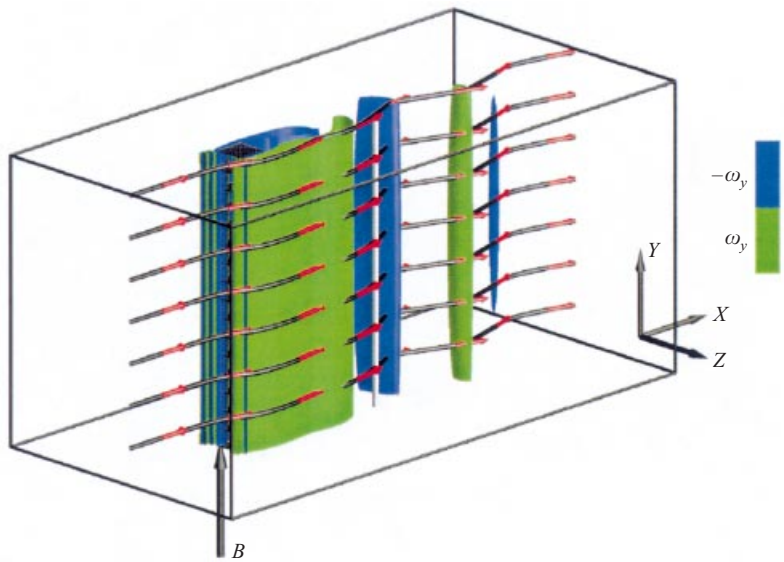


FIGURE 10. Isovorticity surface plot at $Re = 200$, $M = 52.9$, $N = 14$, $\omega_y = \pm 6$; surfaces $\omega_x = \pm 3$ are not present.

of the potential (figure 11) show the connection between flow streamlines and the potential. In figure 11(*b*) the curvature of the potential isolines, which corresponds to the curvature of the vortices, can be seen. A further enhancement of the interaction parameter results in a nearly complete suppression of the vortex shedding at $M = 84.9$ and $N = 36$. The vortex shedding is still present but the vortices are damped almost immediately after they are shed. Since it is difficult to detect exact stability limits with a fully numerical code the end of the vortex shedding was defined at parameters for

https://doi.org/10.1017/S0022112000001300 Published online by Cambridge University Press

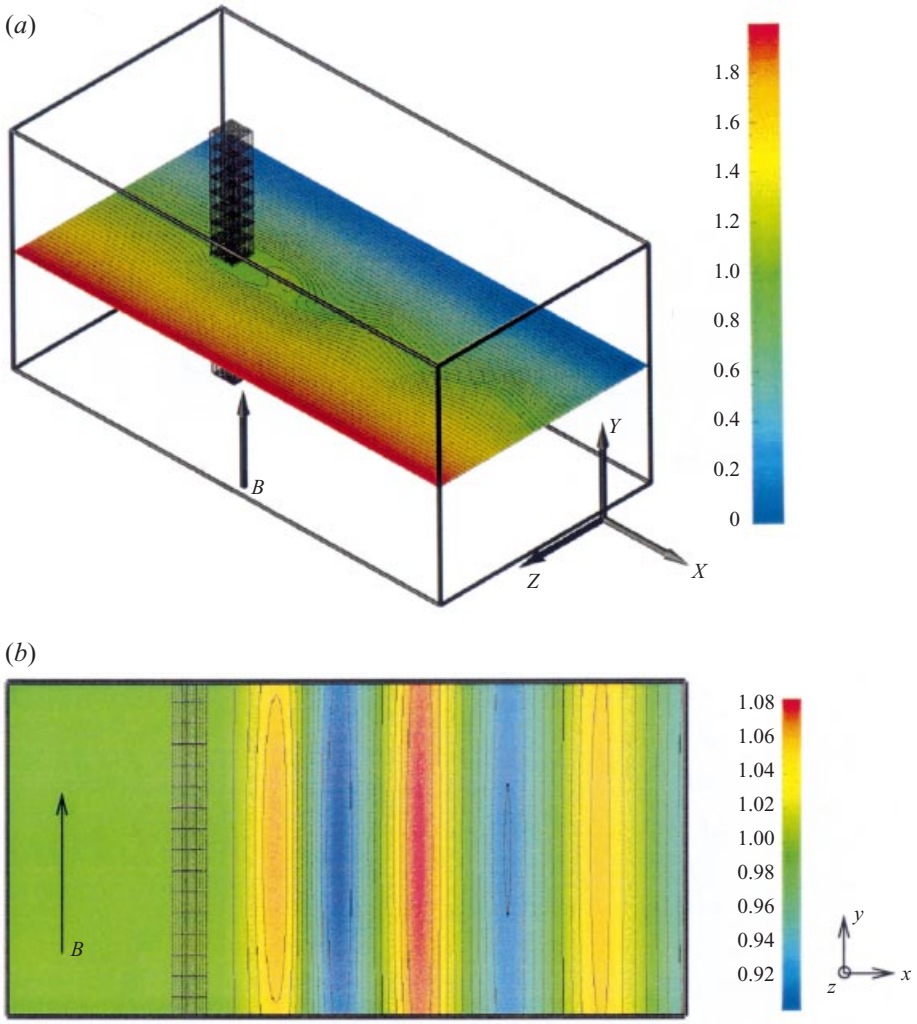


FIGURE 11. Isolines potential plot at $Re = 200$, $M = 52.9$, $N = 14$.

which the level of vorticity at the exit is below a certain threshold. This criterion introduces some uncertainty concerning the end of vortex shedding. Taking equation (7.8) as a qualitative measure one gets $\tau_{Ha}/\tau_c = 1.8$ from the present numerical simulation, which is the correct order of magnitude for the total damping of the vortex street for which $\tau_{Ha}/\tau_c < 1$ has been roughly estimated.

All the results shown so far support the idea of a quasi-two-dimensional MHD flow model at high M and N. With such a model one could investigate the complete damping of the vortex shedding more efficiently than with a three-dimensional code that calculates quasi-two-dimensional flows.

7.3. *Three-dimensional electric currents*

To understand the mechanisms of vortex damping in a channel flow it is essential to know the path of the electric currents. It is then easy to draw conclusions about the Lorentz forces acting on the fluid. The current paths of a MHD flow in a rectangular

https://doi.org/10.1017/S0022112000001300 Published online by Cambridge University Press

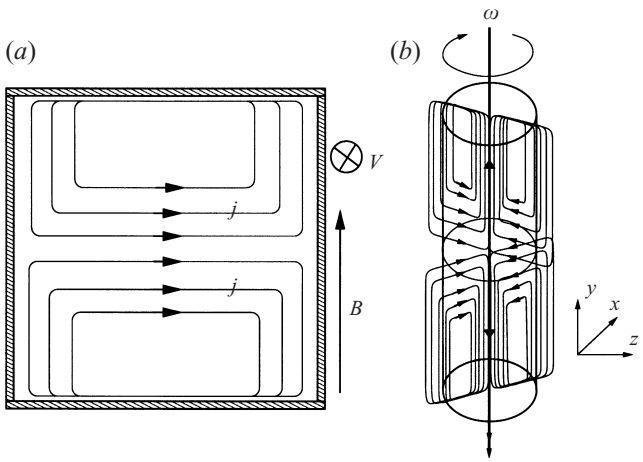


FIGURE 12. Current paths: (*a*) in an insulated channel and (*b*) of a single vortex.

channel are well known, see e.g. Sterl (1990). For an insulated channel the electric currents flow in the transverse section plane of the channel, see figure 12*a*). For a single vortex aligned with the magnetic field between two Hartmann walls located in an non-moving fluid the radially symmetric electric currents close together along the axis of the vortex, see figure 12*b*). The direction of the current depends on the clockwise or anti-clockwise rotation of the vortex. The current paths of a moving vortex in a channel flow is the superposition of the two current patterns. This is shown for clockwise and anti-clockwise rotation in figure 13. For the clockwise rotation (figure 13*a*) outside the vortex the current density is equally distributed over the channel height. In the sphere of the vortex the current is deflected in the direction of the Hartmann walls and the currents partially flow into the Hartmann layer. It will be shown later that the currents entering the Hartmann layer are directly proportional to the core vorticity and thus to the strength of the vortex. On one side of the vortex the current density is increased, on the other side it is reduced resulting in a braking of the rotation of the vortex. For the anti-clockwise rotation (figure 13*b*) the argument is analogous. The electric currents flow approximately in a plane $x = const$ if this plane cuts the vortex exactly into halves. In any other case the current does not flow in one plane but changes its plane in the sphere of the vortex in a direction towards the vortex axis (clockwise rotation) or away from the vortex axis (anti-clockwise rotation).

7.4. *Effects of a magnetic field on the properties of the vortex street*

The only experimental works where the shape of the vortex street has been investigated experimentally are Papailiou (1984) and Frank *et al.* (2000). Papailiou's work was carried out in an open channel with one Hartmann wall missing, so that he could observe the wake of the cylinder on the free surface. Although one can only infer indirectly what is happening under the surface of the liquid metal, one can find qualitative criteria for the action of the magnetic field. He observed that under the action of a magnetic field the wake of the cylinder is narrowed, see figure 14. Additionally he observed that the distance between the vortices in the main flow direction is reduced and the vortices are organized in rows travelling downstream. Concerning the Strouhal number he observed that as long as vortex shedding exists

https://doi.org/10.1017/S0022112000001300 Published online by Cambridge University Press

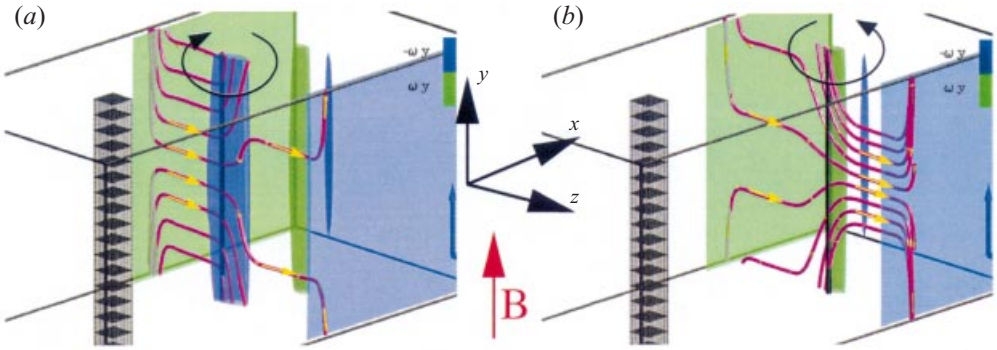


FIGURE 13. Electric current paths of a vortex moving with the flow in an insulated channel. (*a*) Clockwise rotation. (*b*) Anti-clockwise rotation. $Re = 200$, $M = 52.9$, $N = 14$.

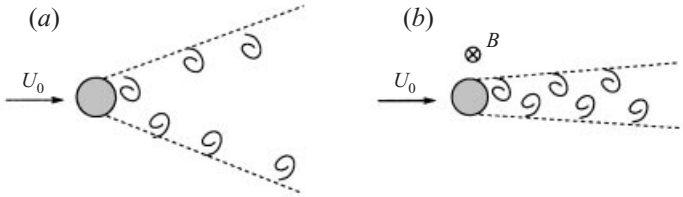


FIGURE 14. Effect of a magnetic field on the wake, following Papailiou: (*a*) no magnetic field, (*b*) with magnetic field.

the effect of a magnetic field aligned with the cylinder on the Strouhal number is weak.

These results were confirmed by the experiments of Frank *et al.* (2000) in a closed insulated channel. With an array of potential probes in the Hartmann walls they could detect the shape of the vortex street. They also found that the wake of the cylinder is narrowed and that the vortices are more organized with a rising magnetic field. They measured a minimal decrease (−0.02) of the Strouhal number when the Hartmann number was doubled at a fixed Reynolds number.

The present numerical simulation confirmed most of the experimental observations. From the plots shown in the previous sections it is clear that the vortex street is strongly organized and the wake is narrowed on the application of a magnetic field. The Strouhal number had a slight tendency to rise with stronger magnetic fields which may be related to the fact that in the simulation a square cylinder was used.

It was also possible to investigate the influence of the magnetic field on the drag and lift forces on the cylinder, see figure 15. It appears that weak and moderate magnetic fields reduce the mean drag until the two-dimensional transition is reached at $N \approx 1$. Then the influence of the MHD pressure losses outweigh other contributions which results in a rising drag coefficient. The RMS value of the lift coefficient is continuously lowered by the action of a magnetic field and should vanish if the lift coefficient ceases to oscillate.

7.5. *Total damping of the vortex street*

The present numerical results were compared with experiments by Frank *et al.* (2000). The blockage ratio of the experiment was the same (10%) as in the present simulation. All walls and the cylinder were insulating. In contrast to the numerical simulation

https://doi.org/10.1017/S0022112000001300 Published online by Cambridge University Press

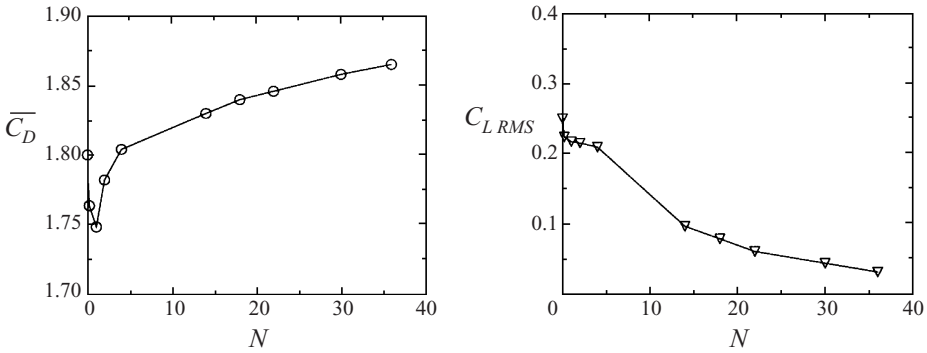


FIGURE 15. Behaviour of mean drag and lift coefficient with rising magnetic field at $Re = 200$.

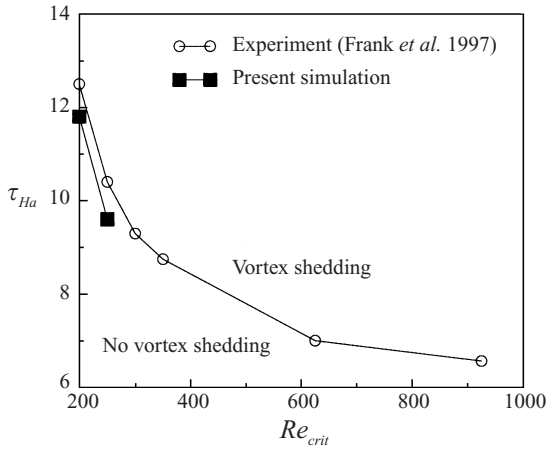


FIGURE 16. Comparison of numerical result and experiment.

a circular cylinder was used in the experiment, so some differences between the experiment and the numerics are expected. However, with the exception of what is happening near the cylinder the action of the magnetic field on the vortices is comparable in both cases.

As explained in § 7.2 for the comparison of MHD vortex damping, typical time scales, e.g equation (7.6) can be used, especially when the aspect ratios of the vortices produced are different. In the experiment an aspect ratio of $\alpha = a/l_\perp = 2.5$ was used whereas in the numerical simulation this ratio was 5. In figure 16 the experimental and numerical results are compared. Due to the excessive consumption of CPU time of this transient three-dimensional problem on a VPP300-16 supercomputer only two Reynolds numbers could be investigated. The numerical simulation shows good agreement with the experiment. The MHD damping needed to suppress the vortex shedding is higher in the numerical simulation. This difference may be explained by the influence of the square cylinder used in the numerical simulation instead of the circular cylinder used in the experiment. Also the definition of the end of vortex shedding shows some uncertainty. However, when taking into account on the one hand the different experimental conditions and experimental uncertainties especially end conditions and on the other hand side effects due to various numerical parameters the agreement does seem to be satisfactory.

https://doi.org/10.1017/S0022112000001300 Published online by Cambridge University Press

A typical feature of quasi-two-dimensional inertial MHD flows, which can be clearly seen in the experimental results in figure 16 is the fact that with increasing Reynolds number the stability limit is increasingly controlled by the value of τ, see also e.g. Bühler (1996). Due to limitations in computer resources it was not possible to reach higher Reynolds numbers with the present three-dimensional numerical simulation to validate this behaviour.

8. Weak inertial effects in quasi-two-dimensional MHD flows

As shown in § 7.2 the vortices aligned with the magnetic field are not strictly two-dimensional but have a slight curvature along the direction of the magnetic field. This curvature is also visible in the potential. In order to explain this effect asymptotic methods are used. The result clearly shows a parabolic variation in the direction of the magnetic field as outlined below. The analysis presented in this section is sufficient to explain the results observed from the numerical simulation.

For our considerations we use the momentum equation (2.1) in the following form:

$$\frac{1}{N}\left[\frac{\partial \boldsymbol{v}}{\partial t} + (\boldsymbol{v}\cdot\nabla)\boldsymbol{v}\right] = -\frac{1}{N}\nabla p + \frac{1}{M^2}\Delta \boldsymbol{v} + (\boldsymbol{j}\times \boldsymbol{e}_y), \tag{8.1}$$

with

$$\nabla\cdot\boldsymbol{v} = 0. \tag{8.2}$$

The elimination of pressure by taking the curl of the momentum equation results in an equation for the vorticity $\boldsymbol{\omega}$:

$$\frac{1}{N}\left[\frac{\partial \boldsymbol{\omega}}{\partial t} + (\boldsymbol{v}\cdot\nabla)\boldsymbol{\omega} - (\boldsymbol{\omega}\cdot\nabla)\boldsymbol{v}\right] = \frac{1}{M^2}\Delta\boldsymbol{\omega} + (\boldsymbol{e}_y\cdot\nabla)\boldsymbol{j}. \tag{8.3}$$

The boundary conditions are the no-slip condition for the velocity at the wall and the thin-wall condition (4.2) which couples the potential at the wall with the wall-normal currents.

8.1. *Analysis*

In terms of vorticity equation (2.5) for potential now reads

$$\nabla^2\Phi = \boldsymbol{\omega}\cdot\boldsymbol{e}_y. \tag{8.4}$$

Considering the y-component of Ohm's law (2.4) it is possible to extract the derivative of the current as it appears in equation (8.3):

$$\frac{\partial j_y}{\partial y} = -\frac{\partial^2\Phi}{\partial y^2} = \nabla_\perp^2\Phi - \omega_y. \tag{8.5}$$

For many applications in MHD inertia effects are very small and can be neglected for strong magnetic fields. However, minor inertia forces can also lead to the formation of time-dependent flow patterns once the laminar flow loses its stability (see e.g. Bühler 1996 or the present work). In the following analysis the inertia is therefore not neglected but the influence is assumed to be weak. This assumption allows a small parameter to be introduced

$$\varepsilon = \frac{1}{N} \ll 1, \tag{8.6}$$

which is useful in an asymptotic expansion of the variables during the analytical treatment of the problem.

https://doi.org/10.1017/S0022112000001300 Published online by Cambridge University Press

It is well known that for strong magnetic fields, when $M \gg 1$ the flow region splits into distinct subregions. One is the core, where viscous effects are negligibly small. Here the flow is mainly governed by a balance of Lorentz forces and pressure forces and eventually small inertia forces. In the other subregions, namely the Hartmann layers and the side layers, the flow is governed by a balance of Lorentz forces and viscous forces. For the purpose of having a single small perturbation parameter that allows one to balance inertia with part of the friction term it is convenient to replace the inverse of the Hartmann number by another small quantity:

$$\frac{1}{M} = \varepsilon h. \tag{8.7}$$

Assume that $h = \alpha/\tau_{Ha}$ does not vanish as $\varepsilon \to 0$. The quantity τ_{Ha} corresponds to the Hartmann braking time (7.6) for the case of insulating walls. Since the walls are assumed to be poorly conducting the wall conductance ratio is replaced by

$$c = \varepsilon C. \tag{8.8}$$

There are two reasons for using a single perturbation parameter ε. One is to keep the analysis as simple as possible to explain the cigar-like shape of the vortices found in the three-dimensional computations. The other reason is that for $N \gg M$ all vortices will disappear quickly by Hartmann braking so that the cigars are hardly observed. For $N \ll M$ Hartmann braking is small and so are the field-aligned currents that create the cigar-like shape. Therefore the condition for which we can observe cigar vortices is that M and N should be of the same order of magnitude. Such an analysis is unable to study the effect of inertia on the Hartmann layers or the transition from three-dimensional to quasi-two-dimensional flows but it explains the unexpected cigar shape of vortices after the transition to a quasi-two-dimensional flow is completed. A more detailed analysis appears in Pothérat, Sommeria & Moreau (2000).

Using these definitions the governing equations for the y-component of $\boldsymbol{\omega}$ in the magnetic field direction is determined by

$$\varepsilon \left[\frac{\partial \omega}{\partial t} + (\boldsymbol{v} \cdot \nabla)\omega - (\boldsymbol{\omega} \cdot \nabla)v \right] = (\varepsilon h)^2 \Delta\omega + \Delta_\perp \Phi - \omega, \tag{8.9}$$

$$\Delta\Phi = \omega. \tag{8.10}$$

For simplicity the subscript y has been dropped. Equation (8.10) is identical to equation (8.4). In the following all variables are expanded in power series of the small quantity ε as

$$\boldsymbol{v} = \boldsymbol{v}_0 + \varepsilon \boldsymbol{v}_1 + \cdots, \tag{8.11}$$

$$\omega = \omega_0 + \varepsilon \omega_1 + \cdots, \tag{8.12}$$

$$\Phi = \Phi_0 + \varepsilon \Phi_1 + \cdots. \tag{8.13}$$

In the core of the flow the leading-order dependence of all fluid variables along the magnetic field lines can be described analytically for many problems. Other important fluid subregions are the Hartmann layers with thickness $\delta \sim M^{-1}$. In the Hartmann layers inertia and pressure forces are of minor importance. The velocity shows a strong variation in the Hartmann layers, dropping from the core value to zero at the wall. The pressure and the electric potential do not have this behaviour in the Hartmann layer. As in Sommeria & Moreau (1982) we do not consider effects of walls parallel to the magnetic field since they are passive in character if they are insulated.

https://doi.org/10.1017/S0022112000001300 Published online by Cambridge University Press

Having in mind that most of the flow obeys inviscid rules, all variables are split into parts that satisfy the equations for the inviscid problem, denoted by a subscript c (core) and a viscous contribution that occurs within the viscous layers denoted by the subscript h (Hartmann layers). The velocity and the vorticity component at the expansion order k are expressed as

$$\boldsymbol{v}_k = \boldsymbol{v}_{ck}(x, y, z, t) + \boldsymbol{v}_{hk}(x, \eta, z, t), \tag{8.14}$$

$$\omega = \omega_{ck}(x, y, z, t) + \omega_{hk}(x, \eta, z, t), \tag{8.15}$$

where

$$\eta = M(y - b) = \frac{1}{\varepsilon h}(y - b) \tag{8.16}$$

is the stretched Hartmann layer coordinate with the Hartmann wall at $\eta = 0$ ($y = b$) and the core at $\eta \to -\infty$. It is known that the viscous correction for the electric potential in the Hartmann layer is small, $O(1/M^2)$, see e.g. Moreau (1990). This is taken into account by expanding the electric potential as follows:

$$\Phi_k = \Phi_{ck}(x, y, z, t) + (\varepsilon h)^2 \Phi_{hk}(x, \eta, z, t). \tag{8.17}$$

Matching with the inviscid solution requires that the viscous corrections of all variables vanish at large distances from the wall as $\eta \to -\infty$.

In the next step all variables are plugged into the y-component of the vorticity equation (8.9) and into the potential equation (8.10). The terms are then collected at equal orders of ε.

8.2. *Leading-order approximation in ε for core variables*

At the leading order in ε which determines the inertialess problem the following equations determine the inviscid core solution.

The y-component of equations (8.9) and (8.10) becomes

$$\Delta_\perp \Phi_{c0} - \omega_{c0} = 0, \tag{8.18}$$

$$\Delta \Phi_{c0} - \omega_{c0} = 0. \tag{8.19}$$

Equation (8.18) and (8.19) differ in

$$\frac{\partial^2 \Phi_{c0}}{\partial y^2} = 0, \tag{8.20}$$

which states that the potential has no variation in the direction of the magnetic field. Equation (8.20) can be integrated twice. With the two-dimensional potential at the Hartmann walls as integration function $\phi(x, z) = \Phi(x, y = b, t, z)$ one finds for y-symmetric problems for the y-component of the electric potential

$$\Phi_{c0} = \phi_0, \tag{8.21}$$

showing that the potential is constant along magnetic field lines at the leading order of approximation. Considering equations (8.10) and (8.20) the vorticity also must be constant in the magnetic field direction at the leading order of approximation

$$\omega_{c0} = \Omega_0. \tag{8.22}$$

8.3. *Leading-order approximation in ε for Hartmann layer variables*

To complete the analysis for the inertialess problem consider the viscous corrections at the leading order. The vorticity equation for viscous corrections leads to an ordinary

https://doi.org/10.1017/S0022112000001300 Published online by Cambridge University Press

differential equation

$$\frac{\partial^2 \omega_{h0}}{\partial \eta^2} - \omega_{h0} = 0. \tag{8.23}$$

The solution satisfying the matching condition with the core and the no-slip condition at the wall is

$$\omega_{h0} = -\Omega_0 \exp(\eta). \tag{8.24}$$

From equation (8.10) one finds for the viscous correction of potential the equation

$$\frac{\partial^2 \Phi_{h0}}{\partial \eta^2} = \omega_{h0}. \tag{8.25}$$

Integrating equation (8.25) leads to the following change of the wall-normal currents due to viscous effects in the Hartmann layer according to Ohm's law (2.4):

$$\frac{\partial \Phi_{h0}}{\partial \eta}(\eta = 0) = \int_{-\infty}^{0} \omega_{h0}\, \mathrm{d}\eta = -\Omega_0. \tag{8.26}$$

8.4. *Order ε for core variables*

By combining the vorticity equation (8.9) and the potential equation (8.10) one finds a relation that governs the inertial but inviscid contribution to the electric potential in the core:

$$-\frac{\partial^2 \Phi_{c1}}{\partial y^2} = \frac{\partial \omega_{c0}}{\partial t} + (v_{c0} \cdot \nabla)\omega_{c0} \doteq D_t \omega_{c0}. \tag{8.27}$$

Since at the leading order the flow is two-dimensional in the core, the right-hand side of equation (8.27) is independent of the direction of the magnetic field. Knowing this one finds immediately that the inertial correction to the electric potential has a parabolic behaviour along magnetic field lines. The final solution is described by an inertialess part independent of y plus a weak inertial correction described by equation (8.27).

This result explains the present numerical solution for the inertial time-dependent vortex shedding with an applied magnetic field. The curvature of the vortices obtained in the present simulation is caused by the weak inertial correction which gives the vortices their cigar-like shape (larger diameter at the centre, smaller diameter near the Hartmann walls). The effect described by equation (8.27) is clearly visible in the potential plot (figure 11*b*). Since the potential is related to the vorticity the effect is also visible in the vorticity (figure 10). One should also recognize that the reduced intensity of the vortices near the Hartmann walls is not created by higher viscous damping in these regions but rather by the inertial contribution to the electric potential in the core flow. Here a parabolic variation of potential along magnetic field lines is found as a weak correction to a quasi-two-dimensional flow. A similar behaviour was found for buoyant MHD flows at leading order of the analysis by Bühler (1998).

The decay of vorticity is determined by applying the thin-wall boundary condition at the Hartmann wall. The electric boundary condition (4.1) involves the potential gradient at the wall. The potential gradient is composed of an inertial and a viscous part. By integration of equation (8.27) the inertial part is obtained:

$$-\frac{\partial \Phi_{c1}}{\partial z}(b) = \int_0^b (D_t \omega_{c0})\, \mathrm{d}z \doteq b\overline{D_t \omega_{c0}}. \tag{8.28}$$

The overbar denotes quantities averaged along magnetic field lines. The viscous part

https://doi.org/10.1017/S0022112000001300 Published online by Cambridge University Press

is obtained from equation (8.26). At the present order of approximation the thin-wall condition results in

$$-h\Omega_0 - b\overline{D_t\omega_{c0}} = c\nabla_\perp^2 \Phi_0. \tag{8.29}$$

It is possible to eliminate the potential with equation (8.22):

$$\overline{D_t\omega_{c0}} = -\frac{1}{\tau^*}\overline{\omega_{c0}} \qquad \text{with} \qquad \tau^* = \frac{b}{h+c}, \tag{8.30}$$

where τ^* is the Hartmann braking time in the case of conducting walls. This equation is equivalent to the quasi-two-dimensional approach of Bühler (1996) that has been obtained by averaging the equations along magnetic field lines. The viscous term due to transverse gradients in vorticity in that reference is not present here at this order of approximation. With insulating walls equation (8.30) is in accordance with that given by Verron & Sommeria (1986) describing the two-dimensional decay of vorticity.

9. Conclusions

The investigation of time-dependent MHD flows becomes important if an improvement in the heat transfer is desired compared with inertialess flow. Additionally there is great interest in the basic physical properties of two-dimensional turbulence which can appear in such flows. Up to now numerical simulations of three-dimensional time-dependent MHD flows have been scarce since the resolution of the thin Hartmann layers is a limiting issue. In the present work this limitation is overcome by applying a model for the Hartmann layer.

The case of the three-dimensional inertial MHD flow around a square cylinder with a magnetic field aligned with the cylinder was investigated. This first numerical simulation of this case confirms previous experimental results and theoretical predictions but also shows a surprising new result, namely that the vortices aligned with the magnetic field are not strictly two-dimensional but have a cigar-like shape.

Using three-dimensional visualizations the physical mechanisms could be shown. It should be noted that the hydrodynamic solution is also of some interest since three-dimensional simulations for this case are rare.

The simulation of the hydrodynamic flow around a square cylinder shows several properties also observed in the first three-dimensional simulations of Sohankar (1998). In this simulation the spatial wake structure for the hydrodynamic case is additionally shown at a Reynolds number of 200 and 250.

After the hydrodynamic flow had reached a fully developed state, the magnetic field was switched on. In the present calculations a transition from a time-dependent three-dimensional flow to a time-dependent quasi-two-dimensional flow occurred at $N \gtrsim 1$ which confirms the experimental findings of Kolesnikov & Tsinober (1972*b*). The feature predicted by Sommeria & Moreau (1982) that the vortices have their ends perpendicular to the Hartmann wall was also confirmed by three-dimensional visualization. For the complete damping of the vortex street a good agreement with the experiments of Frank *et al.* (1997) was achieved.

At interaction parameters above the values for the two-dimensional transition the vortices have a curvature in the direction of the magnetic field, which is also visible in the electric potential. This behaviour was explained by an asymptotic analysis. It appears that the reduced intensity of the vortices near the Hartmann walls is not created by higher viscous damping in these regions but rather by an inertial contribution to the electric potential in the core flow.

https://doi.org/10.1017/S0022112000001300 Published online by Cambridge University Press

To understand the mechanisms of vortex damping the three-dimensional currents in a channel flow with vortices were visualized. It appears that the current pattern for a moving vortex can be seen as a superposition of the current patterns in an insulated channel and those of a vortex between Hartmann walls.

The results of the present simulation show that a vortex street behind a cylindrical insulated obstacle persists over a certain range of parameters under the influence of a magnetic field. The vortex street acquires a state that is close to two-dimensional before it is supressed completely. Such vortex patterns can be produced by several methods and can exist at fusion-relevant parameters, see e.g. Bühler (1996). The two-dimensional state of such vortices can enhance the heat transfer in MHD cooling devices such as self-cooled liquid metal blankets for fusion reactors, see e.g. Burr *et al.* (2000).

The authors would like to thank Professor A. Tsinober for intense discussions and comments during the preparation of this work. This work has been performed in the framework of the Nuclear Fusion Project of the Forschungszentrum Karlsruhe.

REFERENCES

Alboussiére, T., Upenski, V. & Moreau, R. 1999 Quasi-2d MHD turbulent shear layers. *Expl Thermal Fluid Sci.* **20**, 19–24.

Andreev, O. V. & Kolesnikov, Y. 1997 MHD instabilities at transverse flow around a circular cylinder in a axial magnetic field. In *Third Intl Conf. on Transfer Phenomena in Magnetohydrodynamic and Electroconducting Flows, Aussois, France*, pp. 205–210.

Barkley, D. & Henderson, R. 1996 Three-dimensional Floquet stabililty analysis of the wake of a circular cylinder. *J. Fluid Mech.* **322**, 215–241.

Botta, E., Dekker, K., Notay, Y., Ploeg, A. van der, Vuik, C., Wubs, F. & Zeeuw, P. 1997 How fast the Laplace equation was solved in 1995. *Appl. Numer. Maths* **24**, 439–455.

Bühler, L. 1995 Magnetohydrodynamic flows in arbitrary geometries in strong, nonuniform magnetic fields. *Fusion Technol.* **27**, 3–24.

Bühler, L. 1996 Instabilities in quasi-two-dimensional magnetohydrodynamic flows. *J. Fluid Mech.* **326**, 125–150.

Bühler, L. 1998 Laminar buoyant magnetohydrodynamic flow in vertical rectangular ducts. *Phys. Fluids* **10**, 223–236.

Burr, U., Barleon, L., Müller, U. & Tsinober, A. 2000 Turbulent transport of momentum and heat in magnetohydrodynamic rectangular duct flow with strong side wall jets. *J. Fluid Mech.* **406**, 247–279.

Davidson, P. A. 1995 Magnetic damping of jets and vortices. *J. Fluid Mech.* **299**, 153–186.

Davis, R., Moore, E. & Purtell, L. 1984 A numerical-experimental study of confined flow around rectangular cylinders. *Phys. Fluids* **27**, 46–59.

Frank, M., Barleon, L. & Müller, U. 2000 Visual analysis of two-dimensional magnetohydrodynamics. *Phys. Fluids* (in press).

Günther, C. 1992 Conservative versions of the locally exact consistent upwind scheme of second order (LECUSSO-SCHEME). *Intl J. Numer. Meth. Engng* **34**, 793–804.

Henderson, R. 1997 Nonlinear dynamics and pattern formation in turbulent wake transition. *J. Fluid Mech.* **352**, 65–112.

Huerre, P. & Monkewitz, P. 1990 Local and global instabilities in spatially developing flows. *Ann. Rev. Fluid Mech.* **22**, 473–537.

Hunt, J. C. R. & Ludford, G. S. S. 1968 Three-dimensional MHD duct flows with strong transverse magnetic fields Part 1. obstacles in a constant area channel. *J. Fluid Mech.* **33**, 693–714.

Kim, J. & Moin, P. 1985 The fractional step method. *J. Comput. Phys.* **59**, 308–317.

Kit, L., Turuntaev, S. & Tsinober, A. 1970 Investigation with a conducting anemometer of the effect of a magnetic field on disturbances in the wake of a cylinder. *Magnetohydrodynamics* **6** (3), 35–40.

https://doi.org/10.1017/S0022112000001300 Published online by Cambridge University Press

Kolesnikov, Y. & Tsinober, A. 1972*a* An experimental study of two-dimensional turbulence behind a grid. *Fluid Dyn.* **9**, 621–624.

Kolesnikov, Y. & Tsinober, A. 1972*b* Two-dimensional turbulent flow behind a circular cylinder. *Magnetohydrodynamics* **3** (1), 300–307.

Lahjomri, J., Caperan, C. & Alemany, A. 1993 The cylinder wake in a magnetic field aligned with the velocity. *J. Fluid Mech.* **253**, 421–448.

Leboucher, L. 1999 Monotone scheme and boundary conditions for finite volume simulation of magnetohydrodynamic internal flows at high Hartmann number. *J. Comput. Phys.* **150**, 181–198.

Lenhart, L. 1994 Magnetohydrodynamik in Rechteckgeometrien. *Wissenschaftliche Berichte* FZKA 5317. Forschungszentrum Karlsrube.

Malang, S. 1988 Self-cooled liquid metal blanket concept. *Fusion Tech.* **14**, 1343.

Minewitsch, S., Franke, R. & Rodi, W. 1994 Numerical investigation of laminar vortex-shedding flow past a square cylinder oscillating in line with the mean flow. *J. Fluids Struct.* **8**, 787–802.

Molokov, S. & Bühler, L. 1994 Liquid metal flow in a u-bend in a strong magnetic field. *J. Fluid Mech.* **267**, 325–352.

Moreau, R. 1990 *Magnetohydrodynamics*. Kluwer.

Mück, B. 1999 Numerische Untersuchung von Strömungen in Kanälen mit Versperrungen unter dem Einfluß von Magnetfeldern. *Wissenschaftliche Berichte* FZKA 6292. Forschungszentrum Karlsruhe.

Mutschke, G., Gerbeth, G., Shatrov, V. & Tomboulides, A. 1997 Two- and three-dimensional instabilities of the cylinder wake in an aligned magnetic field. *Phys. Fluids* **9**, 3114–3116.

Oertel, H. 1990 Wakes behind blunt bodies. *Ann. Rev. Fluid Mech.* **22**, 539–564.

O'Leary, D. P. & Widlund, O. 1979 Capacitance matrix methods for the Helmholtz equation on general three-dimensional regions. *Math. Comput.* **33** (147), 849–879.

Papailiou, D. D. 1984 Magneto-fluid-mechanic turbulent vortex streets. In *Fourth Beer-Sheva Seminar on MHD Flows and Turbulence*, pp. 152–173. AIAA.

Perot, J. B. 1993 An analysis of the fractional step method. *J. Comput. Phys.* **108**, 51–58.

Persillon, H. & Braza, M. 1998 Physical analysis of the transition to turbulence in the wake of a circular cylinder by three-dimensional Navier–Stokes simulation. *J. Fluid Mech.* **365**, 23–88.

Peyret, R. & Taylor, T. 1983 *Computational Methods for fluid flow*. Springer.

Pothérat, A., Sommeria, J. & Moreau, R. 2000 An effective 2d model for mhd flows with transverse magnetic field. *J. Fluid Mech.* in press.

Sani, R. & Gresho, P. 1994 Résumé and remarks on the open boundary condition minisymposium. *J. Numer. Math: Fluids* **18**, 983–1008.

Shimomura, Y. 1991 Large eddy simulation of magnetohydrodynamic turbulent channel flows under a uniform magnetic field. *Phys. Fluids* A **3**, 3098–3106.

Sohankar, A. 1998 Numerical study of laminar, transitional and turbulent flow past rectangular cylinders. PhD thesis, Chalmers University of Technology, Göteborg.

Sohankar, A., Norberg, C. & Davidson, L. 1997 Numerical simulation of unsteady low-Reynolds number flow around rectangular cylinders at incidence. *J. Wind Engng* **69–71**, 189–201.

Sohankar, A., Norberg, C. & Davidson, L. 1998 Low-Reynolds-number flow around a square cylinder at incidence: study of blockage, onset of vortex shedding and outlet boundary condition. *Intl J. Numer. Meth. Fluids* **26**, 39–56.

Sohankar, A., Norberg, C. & Davidson, L. 1999 Simulation of three-dimensional flow around a square cylinder at moderate Reynolds numbers. *Phys. Fluids* **11**, 288–306.

Sommeria, J. & Moreau, R. 1982 Why, how, and when, MHD turbulence becomes two-dimensional. *J. Fluid Mech.* **118**, 507–518.

Sterl, A. 1990 Numerical simulation of liquid-metal MHD flows in rectangular ducts. *J. Fluid Mech.* **216**, 161–191.

Verron, J. & Sommeria, J. 1986 Numerical simulation of a two-dimensional turbulence in magnetohydrodynamics. *Phys. Fluids* **30**, 732–739.

Walker, J., Ludford, G. & Hunt, J. 1972 Three dimensional MHD duct flows with strong transverse magnetic fields. Part 3. variable-area rectangular ducts with insulating walls. *J. Fluid Mech.* **56**, 121–141.

Walker, J. S. 1981 Magnetohydrodynamic duct flows in rectangular ducts with thin conducting walls I. *J. Méc.* **20**, 79–112.

https://doi.org/10.1017/S0022112000001300 Published online by Cambridge University Press

Williamson, C. 1996 Three dimensional wake transition. *J. Fluid Mech.* **328**, 345–407.

Zhang, H., Noack, B. & Eckelmann, H. 1994 Numerical computation of the three-dimensional cylinder wake. *Bericht* 3/1994. Max-Plank-Institut für Strömungsforschung, Göttingen.

Zikanov, O. & Thess, A. 1998 Direct numerical simulation of forced MHD turbulence at low magnetic Reynolds number. *J. Fluid Mech.* **358**, 299–333.

https://doi.org/10.1017/S0022112000001300 Published online by Cambridge University Press